Simulating Deglacial Radiocarbon Anomalies with pH-neutral Geologic Carbon

R. A. Green[1], P. A. Rafter[3], C. Sun[4], W. R. Gray[5], J. W. B. Rae[6], M. Pelly[6], C. Xu[6], K. Thirumalai[7], J. R. Southon[8], F. Pavia[9], and M. P. Hain[1]

[1] Earth and Planetary Sciences Department, University of Santa Cruz, Santa Cruz, USA

[2] Equatic, Santa Monica, CA, USA

[2] College of Marine Science, University of South Florida, St. Petersburg, FL, USA

[3] Stanford University, Stanford, CA, USA

[4] Laboratoire des Sciences du Climat et de l'Environnement (LSCE/IPSL), Gif-sur-Yvette, France

[5] School of Earth and Environmental Sciences, University of St Andrews, St Andrews, UK

[6] Department of Geosciences, University of Arizona, Tucson, AZ, USA

[7] Department of Earth System Science, University of California Irvine, Irvine, CA, USA.

[8] Department of Oceanography, University of Washington, Seattle, WA 98195, USA

Corresponding author: Ryan A. Green (rygreen@ucsc.edu)

Key Points:

- A regional carbon cycle model shows that geologic carbon release can explain extreme radiocarbon depletion in the eastern tropical Pacific
- Neutralized carbon release matches observations without significantly lowering pH or causing calcium carbonate dissolution
- Radiocarbon remains a reliable ocean circulation tracer when localized carbon sources are accounted for

Abstract

There is currently no explanation or carbon cycle model scenario for severe radiocarbon (^{14}C) depletion reconstructed in the intermediate depth eastern tropical North Pacific Ocean (ETNP) at the end of the last ice age. Here, we develop new constraints on hypothesized geologic carbon release based on the boron isotope pH proxy and regional refinement of a global carbon cycle model. We find that pH-neutral release of ~800 Pg C over 5000 years can produce the radiocarbon anomalies in the ETNP while inducing neither a large pH anomaly nor $CaCO_3$ dissolution (as observed) and causing minimal atmospheric CO_2 rise. Mass-balance considerations dictate that the anomalous carbon was concentrated near the geologic source in

the ETNP without significantly affecting radiocarbon-based reconstructions of global ocean circulation change.

Plain Language Summary

At the end of the last ice age, unusually low levels of radiocarbon were found in ocean waters off the west coast of Mexico. These values are too extreme to be explained by normal ocean circulation. To understand what caused them, we used computer models and chemical records from ancient marine organisms. Our results show that a release of carbon from the seafloor could explain the unusual radiocarbon signals. This release occurred in a part of the ocean that is naturally isolated, which helped trap the carbon and its signal. The carbon was released in a neutralized form, so it didn't cause ocean acidification—consistent with what scientists observe in seafloor fossils. Our findings suggest that these radiocarbon anomalies were caused by a local carbon release into an already isolated region, not by changes in global ocean circulation. This supports the continued use of radiocarbon as a tool for studying past ocean changes.

1 Introduction

The radioactive carbon isotope ^{14}C (radiocarbon) is a key tool for measuring the rate of carbon exchange between the atmosphere and the ocean (Bolin, 1960; Craig, 1957; Revelle & Suess, 1957) and thus provides a powerful constraint on the hypothesis that deep ocean circulation changes drove the abrupt rise in atmospheric carbon dioxide (CO_2) concentrations at the end of the last ice age. In what seemed to be a breakthrough moment, Marchitto et al. (2007) found severe ^{14}C depletions (decay-corrected ^{14}C:^{12}C ratio, expressed as $\Delta^{14}C$; Stuiver & Polach, 1977) in intermediate-depth waters off Baja California in the Eastern Tropical North Pacific (ETNP), potentially explaining the "mystery interval"—a period of rapid atmospheric $\Delta^{14}C$ decline and rising CO_2. Broecker and Barker (2007) proposed that abyssal ocean overturning circulation had stalled during peak glacial conditions, allowing ^{14}C-depleted carbon to accumulate at depth, which was later released during the deglaciation. Subsequent radiocarbon reconstructions and data compilations confirm that deep ocean circulation slowed during the Last Glacial Maximum (LGM) and accelerated during deglaciation, supporting its role in ocean CO_2 release (Rafter et al., 2022; Skinner et al., 2010).

However, the ocean ^{14}C depletions discovered by Marchitto et al. (2007) were found to be too severe and prolonged to be explained by changes in global ocean overturning (Hain et al., 2011). Radiocarbon anomalies have since been reported not only across the Eastern Pacific (Bova et al., 2018; Lindsay et al., 2015; Stott et al., 2009; Stott et al., 2019), but also in the South Pacific (Ronge et al., 2016), the Northwestern Indian Ocean (Bryan et al., 2010) and the North Atlantic (South Iceland Basin and Nordic Seas; Thornalley et al., 2011, 2015). Yet, there remains a particular spatial cluster of anomalies in the ETNP (Lindsay et al., 2016; Marchitto et al., 2007; Rafter et al., 2018, 2019) that have passed tests for species-specific offsets, age model biases, and the impacts of bioturbation (Rafter et al., 2018) (Fig. 1). These sites exist alongside equatorial-located records that show no such anomalies (Bova et al., 2018; Chen et al., 2020), raising a significant problem for the paleoceanographic research community: if ocean

circulation did not cause the radiocarbon anomalies, how reliable are radiocarbon-based reconstructions of ocean circulation?

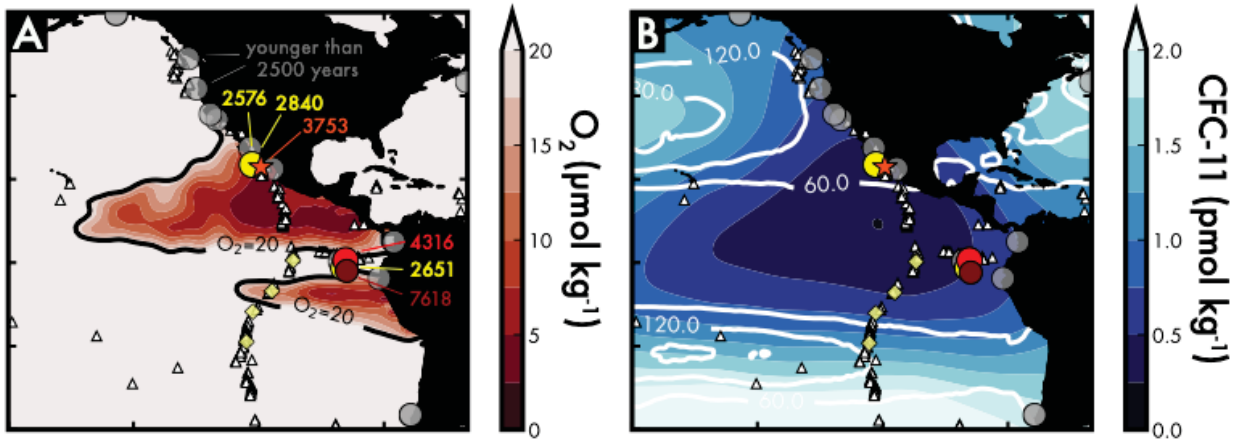

Figure 1. *Intermediate depth (<1000 m) ^{14}C anomalies (colored points: Bova et al., 2018; Marchitto et al., 2007; Rafter et al., 2018, 2019; Stott et al., 2009; Stott et al., 2019) in the context of modern Eastern Pacific hydrographic conditions. Anomalies are defined as having mean deglacial (18 kyr BP-12 kyr BP) ventilation ages >2500 years, with data collected from the Rafter et al. (2022) ^{14}C compilation. The age of each anomaly record is shown in the plot. Non-anomalous ^{14}C data is shown in grey. The star marks the site of new data presented in this study. Subplot (a) shows dissolved O_2 (µmol kg^{-1}) at 500 meters depth (Garcia et al., 2023), while (b) shows concentrations of chlorofluorocarbons (CFC-11 in pmol/kg) and white contours of potential vorticity (10^{-12} m^{-1} s^{-1}) at 500 meters depth (Lauvset et al., 2024). Both maps indicate the locations of hydrothermal vents, represented by white triangles. Yellow diamonds mark East Pacific Rise core sites which document elevated hydrothermal metal fluxes during the deglaciation (Frank et al., 1994; Lund et al., 2016; Lund et al., 2019).*

One proposed solution is that the anomalies are due to unspecified diagenetic overprints erasing the primary seawater radiocarbon signature. However, the sampled benthic and planktonic foraminifera data in the ETNP pass a wide range of preservation tests, show replication on multiple benthic foraminifera species, and are built on a high-quality sedimentary age model (based on ^{14}C-dated terrestrial wood fragments; Rafter et al., 2018) (Fig. 3d). One specific concern is the possibility of overgrowth of authigenic carbonate on foraminiferal tests, associated with sediment porewater sulfate reduction horizons, which can alter foraminifera ^{14}C ages in northwest Pacific sediments (Cook et al., 2011). If these $\Delta^{14}C$ anomalies were driven by sulfate reduction, we would expect them at similar sediment depths along the same redox horizon. Instead, the anomalies are found in sediments of the same geological age but at varying depths (Marchitto et al., 2007; Rafter et al., 2018). This coincidence could be explained by active sulfate reduction in surface mixed-layer sediments during the anomalous periods, possibly driven by transient intensification of oxygen-deficient denitrification zones in the eastern tropical Pacific during the deglacial period (Studer et al., 2021). However, a dilution of foraminiferal calcite greater than 20% needed to produce a 200‰ radiocarbon anomaly would be visible upon inspection of the picked foraminiferal samples and moreover, their stable isotopic composition would reveal the poor preservation state of the tests–neither of which are

observed (Cook & Keigwin, 2015; Rafter et al., 2018). As such, we lack any sound basis to discount the ETNP radiocarbon anomalies, posing a challenge to interpreting other spatially isolated deglacial radiocarbon anomalies, such as those offshore Oman (Bryan et al., 2010) and the Galapagos (Stott et al., 2009).

We investigate an alternative explanation for the deglacial radiocarbon anomalies: a release of ^{14}C-free carbon from geologic sources on the ETNP seafloor (Lund & Asimow, 2011; Rafter et al., 2019; Ronge et al., 2016; Stott et al., 2009; Stott et al., 2019; Stott & Timmermann, 2011), possibly related to climate-paced variability in seafloor spreading and volcanism (Huybers & Langmuir, 2009; Lund et al., 2016; Lund et al., 2019; Lund & Asimow, 2011). Independent evidence for enhanced hydrothermal activity during deglaciation is also provided by ridge-crest sediment records of metal fluxes along the EPR (Frank et al., 1994; Lund et al., 2016; Lund et al., 2019). In this hypothesized scenario, the anomalous foraminiferal samples grew in seawater with admixed geologic carbon. Some proponents of this hypothesis suggest the geologic carbon was released in the form of CO_2, contributing to the deglacial rise of atmospheric CO_2 (Ronge et al., 2016; Stott et al., 2009; Stott et al., 2019; Stott & Timmermann, 2011). However, significant CO_2 release would have lowered seawater pH and reduced carbonate ion (CO_3^{2-}) concentrations and $CaCO_3$ saturation, causing partial or complete dissolution of the anomalous foraminifera material—which instead appears well preserved (Lindsay et al., 2015; Marchitto et al., 2007; Rafter et al., 2018, 2019; L. Stott et al., 2009).

More recently, Rafter et al. (2019) proposed that the geologic carbon was instead neutralized by an equimolar amount of alkalinity, converting the CO_2 to bicarbonate (HCO_3^-) and mitigating localized seawater acidification. Such alkalinity could plausibly be supplied by carbonate mineral dissolution, consistent with the limited $\delta^{13}C$ shift associated with neutralized geologic carbon addition (Green et al., 2024; Fig. S1), though basalt alteration or other water–rock reactions may also have contributed. Further, inverse carbon cycle modeling based on reconstructed atmospheric CO_2 and $\Delta^{14}C$ records suggests that geologic carbon release was unlikely to exceed ~800 Pg C and must have been accompanied by a comparable input of alkalinity (Green et al., 2024). However, this scenario fails to produce basin-scale $\Delta^{14}C$ anomalies due to the rapid dissipation of the $\Delta^{14}C$ signal within the global carbon cycle (Green et al., 2024; Hain et al., 2011).

In this study, we directly assimilate the anomalous ETNP $\Delta^{14}C$ data to infer the required carbon release in a refined model representation of the Gulf of California (GoC) region with varying degrees of hydrographic isolation. We also present new benthic and planktic foraminiferal boron isotope data ($\delta^{11}B$, a proxy for seawater pH), measured on the same samples and over the same interval as the observed ^{14}C-depletions. These data allow us to constrain the carbonate system perturbation associated with the ^{14}C-depletions and determine the concomitant alkalinity inputs.

2 Materials and Methods

2.1 Model details

2.1.1 ETNP regional model

To simulate geologic carbon addition in the Eastern Tropical North Pacific (ETNP), we developed a regional three-box carbon cycle model specifically tailored to this region. The model comprises three connected boxes: (1) the intermediate-depth ETNP shadow zone, which interacts with the Gulf of California (GoC) via the Mexican Coastal Current (MCC; Gómez-Valdivia et al., 2015), (2) the northward-flowing subsurface GoC waters, and (3) the southward-flowing surface waters in the GoC. These are referred to as the "Marchitto box" (in reference to the original discovery of the $\Delta^{14}C$ anomalies; Marchitto et al., 2007), the "GoC subsurface box," and the "GoC surface box", respectively (Fig. 2). Within these boxes we optimize for carbon and alkalinity fluxes to replicate the observed $\Delta^{14}C$ anomalies (Marchitto et al., 2007; Rafter et al., 2018, 2019).

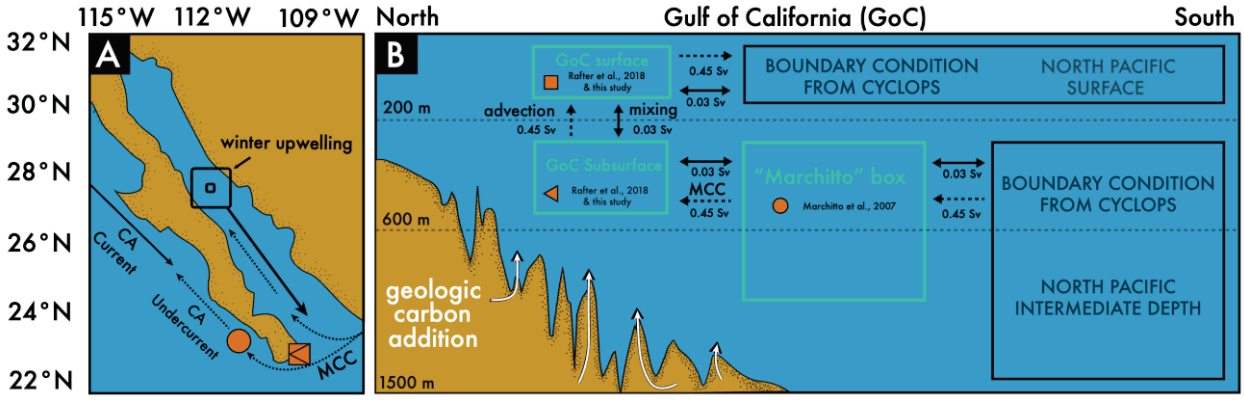

Figure 2. *Regional model framework and observational data used to inform the model. Mean Gulf circulation is estuarine: in at depth and out at the surface (dashed arrows; Lavín & Marinone, 2003). The regional model framework is shown by the teal boxes (panel b). The model's boundary conditions come from the global carbon cycle model, CYCLOPS, and are shown with black boxes (panel b). Markers indicate the location of proxy data used in this study, from the California Undercurrent (orange circle) and Gulf of California (orange sideways triange and square) site LPAZ-21P (a and b). In panel b, the markers are shown in each box corresponding to which data informs which box in the regional model. In panel a, there are two markers for the Gulf of California site LPAZ-21P because the core site includes planktic and benthic data. Note that the subsurface (200 to ≈700 m) Mexican Coastal Current (MCC) feeds into the deep Gulf and California Undercurrent (Gómez-Valdivia et al., 2015), bathing both the Gulf and Undercurrent core sites (Marchitto et al., 2007), thus the Undercurrent core site (orange circle) can be assumed representative of water "upstream" to the Gulf of California core site. Figure is adapted from Rafter et al. (2019).*

The GoC subsurface and surface boxes are assigned depths of 600 meters and 200 meters, respectively, with the subsurface depth based on benthic radiocarbon records found at 624

meters (Rafter et al., 2018) and the surface depth based on Lavín and Marinone (2003). The northern boundary is defined at the Guaymas Basin, where upwelling occurs approximately 550 km north of the GoC core site (Rafter et al., 2019). The model's GoC box width is set to 150 km, following Nix (2013).

Given the uncertainty in the spatial extent and relative isolation of the ^{14}C-depleted water mass entering the GoC, we conduct experiments across a range of Marchitto box sizes (0.01 to 10 times the GoC volume) and mixing rates (0.01 to 5 Sverdrups (Sv), where 1 Sv = 10^6 m^3 s^{-1}; Fig 4a). We highlight two end-member cases: a "fast-flushing" scenario with high mixing (4.7 Sv) and a smaller box (5.6 times the GoC), and a "slow-flushing" scenario with low mixing (0.5 Sv) and a larger box (9.65 times the GoC). These scenarios capture how varying degrees of regional isolation affect the amount of carbon release needed to produce the reconstructed $\Delta^{14}C$ signals. Within the regional model, advection is set at 0.45 Sv based on Rafter et al. (2019), correcting a typographical error in the original manuscript that reported 0.3 Sv. Mixing within the GoC is assigned a rate of 0.03 Sv, an initial estimate approximately 15 times smaller than the advection flux. Further details on model parameters can be found in Figure 2.

2.1.2 Coupling with CYCLOPS

To incorporate global carbon cycle dynamics, we coupled this regional model with the CYCLOPS global carbon cycle model (Green et al., 2024; Hain et al., 2011, 2014) through an iterative process of asynchronous model coupling. The control run simulates background deglacial conditions with no geologic carbon addition (Hain et al., 2014).

The regional GoC model is initially forced using CYCLOPS control simulation results, including P, DIC, ALK, $\Delta^{14}C$, and $\delta^{13}C$ concentrations. Optimization of geologic carbon addition to the GoC regional model is conducted using the minimize function from the SciPy library (Virtanen et al., 2020), ensuring that simulated $\Delta^{14}C$ values remain within a threshold of 0.1‰ of observations. Boundary fluxes diagnosed from the optimized GoC model are then applied as a forcing to the global CYCLOPS model to adjust the boundary condition for the GoC to be consistent with the simulated carbon and alkalinity release. With each iteration of this process the models exchange outputs so as to maintain chemical and isotopic mass balance, ensuring that both regional and global carbon cycle processes are captured. The iterative process continues until the boundary fluxes and geologic carbon release converge on a stable solution, within 1 Pg C over two consecutive runs. In most simulations presented in the main text, geologic carbon is added with an equimolar amount of alkalinity (ALK:DIC ratio of 1:1, simulating bicarbonate addition) and a $\delta^{13}C$ value of -2.5‰, based on Green et al. (2024). To explore other potential sources of geologic carbon, we also simulate the slow-flushing scenario with geologic carbon added as pure CO_2 (ALK:DIC ratio of 0) and a $\delta^{13}C$ value of -8.9‰, based on the mean $\delta^{13}C$ of CO_2 collected from hydrothermal vents in the GoC by Paduan et al. (2018) (Fig. S1c). Because the CYCLOPS control simulation underestimates baseline $\Delta^{14}C$ in the intermediate North Pacific relative to the observations, the boundary conditions imposed on the ETNP model are slightly too low before optimization. As a result, simulated anomalies are muted compared to the data. If the baseline $\Delta^{14}C$ were higher, a larger anomaly would be required, implying either greater

isolation or higher geologic carbon fluxes. Because both regional ocean circulation and the rate of geologic carbon release influence the relationship between rate and resulting 14C signal, both factors will be analyzed and discussed below.

2.1.3 $\Delta^{14}C$ data assimilated with the regional model

Our regional model framework is informed by $\Delta^{14}C$ data from benthic and planktic foraminifera collected at the mouth of the GoC and along the Pacific margin of Baja California. For the GoC, benthic and planktic foraminiferal data were gathered from a depth of 624 meters (Rafter et al., 2019). The subsurface $\Delta^{14}C$ record was built using benthic foraminifera species *Planulina ariminensis* and *Uvigerina* spp., both of which are good recorders of bottom water $\Delta^{14}C$ (Rafter et al., 2018). The surface water $\Delta^{14}C$ record was built by measuring the planktic foraminifera species *Globigerina bulloides*. For years with multiple benthic records, we used the average $\Delta^{14}C$ value of both species to provide a representative estimate.

The GoC core site is influenced by the MCC, which transports poorly ventilated subsurface waters northward (Gómez-Valdivia et al., 2015). This current also supplies water to the California Undercurrent, overlying sediment core sites along the Pacific margin of Baja California, where the earliest deglacial $\Delta^{14}C$ anomalies were observed (Marchitto et al., 2007). Accordingly, we use the mixed benthic foraminiferal record from California Undercurrent waters (Marchitto et al., 2007) as a proxy for conditions in the MCC and the ETNP shadow zone (i.e., the Marchitto box; see Fig. 2). The GoC follows an estuarine circulation pattern, with deep inflowing seawater and surface outflow. Within this structure, benthic foraminiferal data represent the characteristics of poorly ventilated subsurface inflow from the MCC, while planktic foraminifera reflect the outflowing surface water conditions (i.e., the GoC boxes; see Fig. 2).

In addition to $\Delta^{14}C$, we also measured $\delta^{13}C$ and $\delta^{11}B$ from the same sediment core as the GoC $\Delta^{14}C$ anomalies (Rafter et al., 2018, 2019), derived from the benthic foraminifera *P. ariminensis*. These additional isotopic records provide further insights into the past carbonate chemistry and water mass characteristics of the ETNP, supplementing the $\Delta^{14}C$ data used to inform the model.

In our framework, all $\Delta^{14}C$ records (from the Marchitto box and the Gulf of California; Marchitto et al., 2007; Rafter et al., 2018, 2019) are assimilated to optimize the required geologic carbon release under different flushing scenarios. By contrast, $\delta^{13}C$ and $\delta^{11}B$ data from the Gulf of California core are not assimilated and therefore provide independent validation of the modeled carbonate system response.

2.2 Proxy data

2.2.1 $\delta^{11}B$ analytical methods and ΔpH calculations

Between 4-8 benthic and > 50 planktic foraminiferraa tests were picked from the >250 mm and >125 mm size fraction for trace element and boron isotope ($\delta^{11}B$) analyses. Sample preparations were carried out in a low-boron clean lab at the University of St Andrews. Samples

were cleaned based on the "Mg-cleaning" oxidation procedure (Barker et al., 2003; Rae et al., 2011). An aliquot (~3% of the total sample) was taken for trace element analyses, which were performed on an Agilent 8900 ICP-MS at the University of St Andrews using matrix-matched standards. Long-term reproducibility of Mg/Ca and B/Ca using this method is 1.2% and 2.3% (2 SD), respectively. Prior to $\delta^{11}B$ analysis, samples were screened for potential contamination by checking various elemental ratios (B/Ca, Mg/Ca, and Al/Ca). All samples have Al/Ca ratios <100 µmol/mol.

Boron was separated from the sample matrix using Amberlite IRA-743 boron specific anion exchange resin. For one set of samples, the protocol followed the 'column' method of Foster (2008) and Foster et al. (2013). For a subsequent set of samples, the 'batch' protocol of Trudgill et al. (2024) was used, which improves the precision of $\delta^{11}B$ analysis at low concentrations typical of foraminiferal samples. Analysis of the same standard by both techniques shows no significant offset between the techniques (Trudgill et al., 2024 and below).

$\delta^{11}B$ was measured on a Thermo Scientific Neptune plus MC-ICP-MS at the University of St Andrews, based on protocols described in Foster (2008), Rae et al. (2011), Rae (2018), but with the addition of high ohmage (10^{13} Ω) resistors and triplicate sample analyses (Trudgill et al., 2024; Xu et al., 2024). Samples were corrected for total procedural blank, which averaged 80 pg for the samples for through columns, and ~9 pg for the samples analyzed by batch.

Rae et al. (2011) previously reported uncertainties of ±0.23‰ (2 SD) for samples of ~20 ng, increasing at smaller sample sizes. This has been improved given the developments in analyses described above (Trudgill et al., 2024). For example a boric acid standard (ERM-AE121; Vogl & Rosner, 2012) run during these sessions at a similar concentration and under the same conditions as these samples (15-25 ppb) gave $\delta^{11}B$ = 19.64 ±0.06‰ (2 SD, *n* = 8). However as full description and quantification of this updated method is beyond the scope of the current study, we assign conservative analytical uncertainties following the relationships in Rae et al. (2011) for the samples analysed through columns. For the samples analyzed by batch (which improves the precision of small samples relative to columns), we assign the external standard deviation of repeated analysis of NIST 8301 Foram (spanning the sample size range of the foraminiferal samples) by this method during the analytical session (±0.11 ‰ 2SD, n=5), which agrees with the long-term reproducibility of the method within the lab as reported by Trudgill et al. (Trudgill et al., 2024) in size range spanning the samples.

Replicate purifications and measurements of NIST 8301 Foram (a dissolved carbonate standard with a composition mimicking planktic foraminifera), analyzed during the same analytical sessions as the samples, gave a value and ±2 SD of 14.72±0.23‰ (*n* = 2) using the columns method at 25 ppb, and 14.63±0.11 ‰ (*n* = 5) at 15 ppb using the batch method. Thus, no significant difference between the methods is evident.

We reconstructed pH from the $\delta^{11}B$ measurements using the established boron isotope-pH proxy (Zeebe & Wolf-Gladrow, 2001):

$$pH_0 = pK_B - log_{10}\left(\frac{\delta_0 - \delta_{SW}}{\delta_{SW} - \alpha \times \delta_0 - \epsilon}\right)$$

Here, ϵ and α are the equilibrium boron isotope effect and fractionation factor (i.e., 27.2‰ and 1.0272; see Klochko et al. (2006). δ_{SW} represents the boron isotopic composition of bulk seawater, for which we use 39.61‰, and δ_0 is the reconstructed boron isotopic composition of borate from which pH is calculated. pK_B is the borate/boric acid equilibrium constant, which is temperature and salinity dependent (Dickson, 1990). For calculating pK_B, we use mean ocean temperature reconstructions (Bereiter et al., 2018) and a constant salinity of 35 PSU.

Relative pH changes (Fig. 4 and 5) was calculated as the deviation of individual pH estimates (pH_0) from the mean reconstructed pH across all $\delta^{11}B$ measurements. To account for uncertainties, we propagated errors from the $\delta^{11}B$ measurements (±1σ) and temperature (±1 ˚K) on pK_B, yielding 1σ error bars for the pH reconstructions.

2.2.2 $\delta^{13}C$ analytical methods

Benthic $\delta^{13}C$ measurements of *P. ariminensis* were performed on a Thermo Kiel IV Carbonate Device connected to a Thermo MAT 253+ Isotope Ratio Mass Spectrometer at the Paleo² Laboratory at the University of Arizona. The $\delta^{13}C$ data are reported in permil notation relative to the Vienna Pee Dee Belemnite scale (‰, VPDB). IAEA-603 was analyzed (n=40) as an external standard, and the 1σ precision was 0.05‰ for ^{13}C, which is consistent with the long-term precision of this setup (0.05‰; n>1500).

2.2.3 CFC-11 interpolation

To characterize the distribution of CFC-11 in the ETNP, we used data from the GLODAPv2 2023 dataset (Lauvset et al., 2024). Observational points within the ETNP were filtered for CFC-11 values at depths closest to 500 meters, then interpolated across a 2D grid using Ordinary Kriging with a linear variogram model, creating a continuous spatial representation of CFC-11 concentrations (Fig. 1b).

3 Results

3.1 Simulating the ETNP $\Delta^{14}C$ anomalies

The ETNP $\Delta^{14}C$ anomalies (Lindsay et al., 2016; Marchitto et al., 2007; Rafter et al., 2018, 2019) (Fig. 1a) are situated in a 'shadow zone' of the geostrophic flow of the North Pacific gyre, where potential vorticity barriers limit exchange between the ETNP and the open Pacific. This hydrodynamic isolation coincides with low oxygen concentrations and weak intrusion of anthropogenic CFC-11 (Fig. 1a and 1b), making it a plausible site for localized radiocarbon depletion.

We assess the impact of hydrodynamic isolation using our coupled regional-global box model (Section 2.1), in which we systematically vary the volume of the Marchitto box and its boundary

exchange fluxes with the open ocean as simulated by the global CYCLOPS model. Here, we focus on two illustrative end-member scenarios that span a plausible range of conditions: (1) a "fast-flushing" case (red symbols in Figs. 3 and 4) with high exchange (~5 Sv) and small volume (~5x GoC), and (2) a slow-flushing case (yellow symbols in Figs. 3 and 4) with low mixing (~0.5 Sv) and larger volume (~10x GoC). In the Marchitto box, the slow-flushing scenario requires 393 Pg C to match the observed $\Delta^{14}C$ anomalies, compared to 1845 Pg C for the fast-flushing case (Fig. 3c). Downstream, inside the GoC, both scenarios converge on ~600 Pg C needed to reproduce the $\Delta^{14}C$ signals in the GoC subsurface and surface boxes (Fig. 3a, b). The total carbon added for both end-member scenarios broadly align with the conservative (~800 Pg C) and speculative (~2400 Pg C) upper bounds from the global radiocarbon budget (Green et al., 2024) (Fig. 3a).

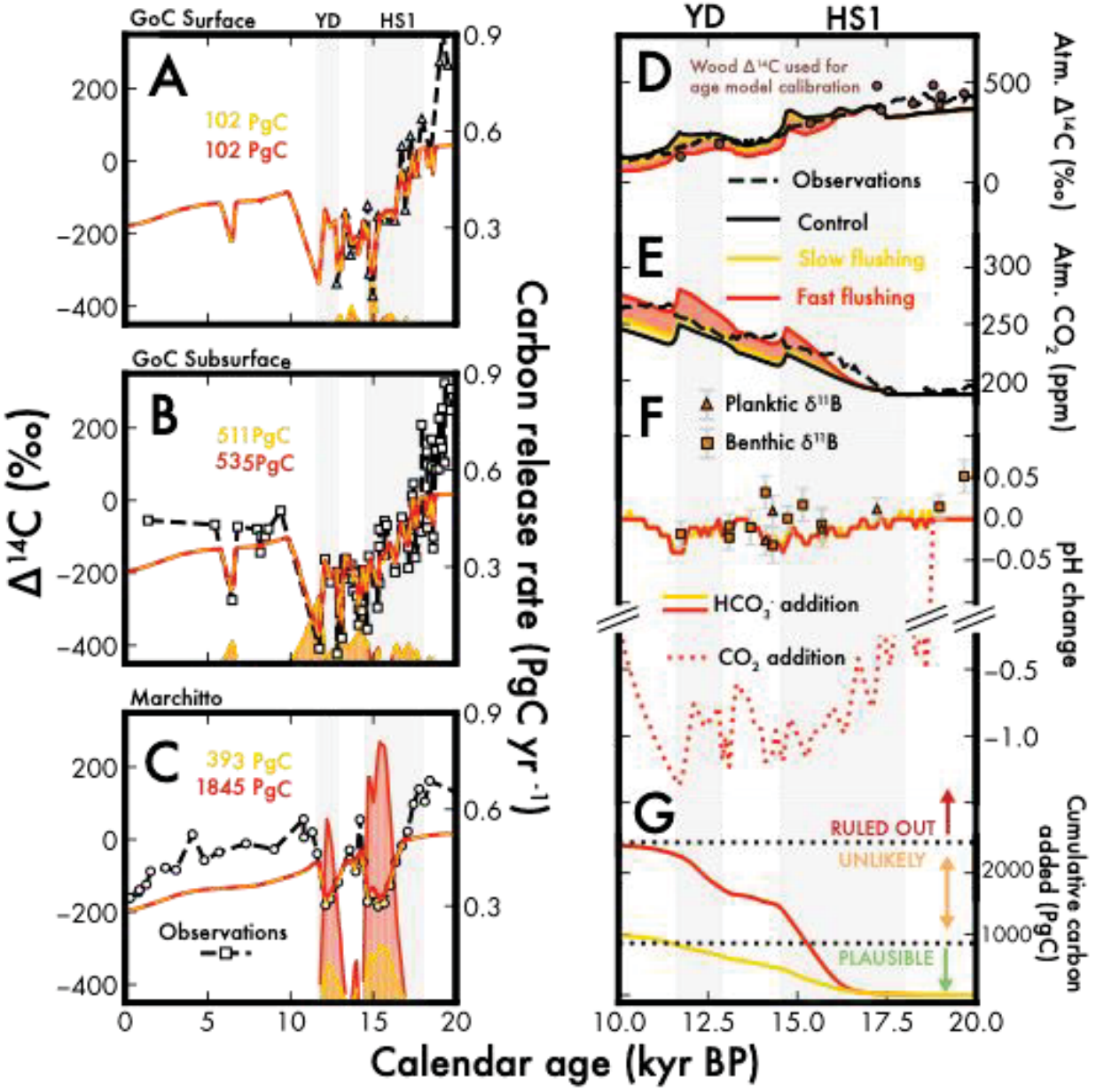

332

Figure 3. *Comparison of simulated and observed ^{14}C anomalies, atmospheric data, and pH change, with modeled geologic carbon release rates for both slow and fast flushing experiments. Panels a–c display the simulated $\Delta^{14}C$ anomalies and release rates for the Marchitto box (panel c), the GoC subsurface (panel b) and the surface (panel a), with observational $\Delta^{14}C$ data shown as markers: circles for the Marchitto box (Marchitto et al., 2007), squares for GoC subsurface* (Rafter et al., 2018) *(benthic), and triangles for GoC surface* (Rafter et al., 2018; *planktic*). *Simulated $\Delta^{14}C$ results are shown as lines with shaded areas representing release rates. Yellow and red correspond to the slow and fast flushing experiments, respectively. Panel d and e display atmospheric $\Delta^{14}C$* (Reimer et al., 2020) *and CO_2* (Bereiter et al., 2015), *respectively, alongside simulated results. The simulated results are shown relative to a control run based on the deglacial carbon cycle scenario from Hain et al*. (2014). *Wood $\Delta^{14}C$ data is shown with brown circles, which was used for calibrating the age model in Rafter et al.* (2018, 2019) *and the new data from this study. Panel f shows the observed pH change (derived from $\delta^{11}B$ data, with 1σ uncertainty indicated by error bars) and simulated pH change. Panel g displays cumulative carbon addition, with dashed black lines showing constraints based on the global radiocarbon budget* (Green et al., 2024).

The large difference in total carbon released between the two end-member scenarios offers a useful contrast when comparing to reconstructed atmospheric $\Delta^{14}C$, CO_2, and regional pH data. The fast-flushing experiment, which releases 2482 Pg C, slightly undershoots reconstructed atmospheric $\Delta^{14}C$. This discrepancy is consistent with a possible bias in the simulated ^{14}C production history before the LGM (Green et al., 2024). Additionally, it overshoots reconstructed CO_2, related to the fixed equimolar carbon and alkalinity flux used to match the ETNP $\Delta^{14}C$ anomalies. The slow-flushing scenario better fits atmospheric $\Delta^{14}C$ and CO_2, though both scenarios are broadly consistent with these data considering uncertainties in the ^{14}C budget and the assumed carbon-to-alkalinity ratio. The similarity in CO_2 histories across two vastly different carbon cycle scenarios arises because equimolar carbon and alkalinity release have minimal impact on seawater pH, confirmed by the small pH change in our reconstructions for the GoC site (Fig. 3f, 4b) based on epifaunal benthic foraminifera.

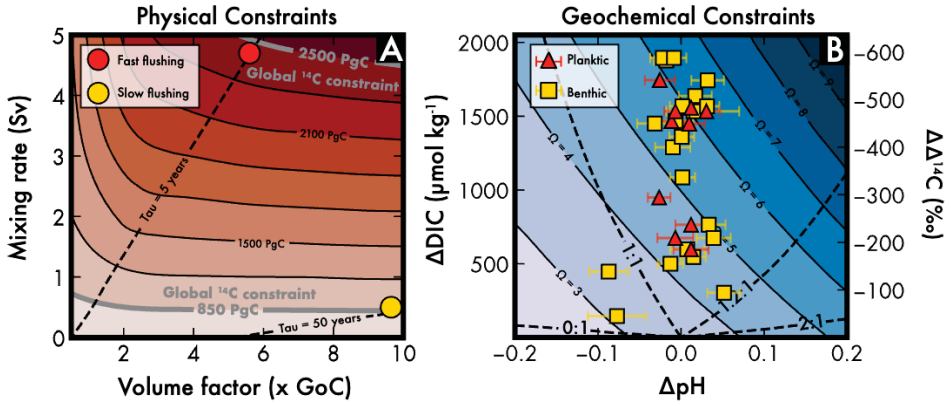

Figure 4. *Physical and geochemical constraints on geologic carbon addition. (a) Physical constraints showing simulated carbon release across a range of mixing rates (y-axis) and Marchitto Box sizes (x-axis, in multiples of GoC volume). Contours represent the total carbon*

required simulate $\Delta^{14}C$ anomalies, with gray lines indicating global radiocarbon budget limits (Green et al., 2024). *Yellow and red circles denote slow and fast flushing end-member experiments, respectively, with black dashed lines showing their respective residence times of the Marchitto box. (b) Geochemical constraints based on PyCO2SYS* (Humphreys et al., 2021) *solver results and observations. Unlike Figure 3f, which covers the 20–10 ka interval, Figure 4b includes the full $\delta^{11}B$-derived pH dataset extending back to 35 ka; no interpolation was applied. We apply a scaling relationship between ^{14}C-free carbon addition and resulting $\Delta^{14}C$ anomalies from the CYCLOPS carbon cycle model ($\Delta\Delta^{14}C$ = -0.31 * ΔDIC) to align PyCO2SYS-derived aragonite saturation state (Ω) contours with calculated ΔpH and $\Delta\Delta^{14}C$ from observed GoC data spanning 35 kyr to 11 kyr BP (yellow squares for benthic and red triangles for planktic). 1σ error bars are shown for the pH reconstruction derived from $\delta^{11}B$. Ω contours are calculated from a range of DIC and pH values, assuming a baseline DIC concentration of 2150 µmol kg^{-1} and a pH of 8.07. Dashed black lines indicate ALK:DIC ratios for different hypothetical geologic carbon sources. Collectively, the $\delta^{11}B$ and $\Delta^{14}C$ data are consistent with an ALK:DIC ratio in the range of 1.0–1.2, similar to the constant ratio of 1 used in our simulations and the mean ratio of ~1.1 estimated by Green et al. (2024). For all ratios in this range, $CaCO_3$ saturation (Ω) increases with carbon addition, consistent with the observed preservation of foraminiferal tests.*

If the carbon were released as pure CO_2 without alkalinity, it would lead to substantial local acidification and elevated atmospheric CO_2 levels. In our slow-flushing scenario, pure CO_2 addition results in a sustained pH drop of more than 1 unit throughout the deglacial period–far exceeding the minor pH change (~0.05) observed in $\delta^{11}B$-derived data (Fig. 3F, Fig. S1b) , which, although lower in temporal resolution than the $\Delta^{14}C$ record, shows no evidence of short-term acidification. To generate the observed $\Delta^{14}C$ anomalies without deviating from this pH constraint, the geologic carbon must have an alkalinity-to-dissolved inorganic carbon (ALK:DIC) ratio between 1:1 and 1.2:1 (Fig. 4b). Pure CO_2 addition (ALK:DIC of 0:1) immediately drives unobserved acidification before producing any notable $\Delta^{14}C$ anomaly. Additionally, CO_2 addition would cause atmospheric CO_2 levels to greatly overshoot reconstructed values, reaching approximately 300 ppm by ~12-kyr BP (Fig. S1a).

4 Discussion

4.1 Role of hydrodynamic isolation

While geologic carbon release is expected to drive localized $\Delta^{14}C$ anomalies, previous attempts to simulate such anomalies in the equatorial and South Pacific have failed, even with carbon release rates comparable to our high-flushing scenario (Ronge et al., 2016; Stott et al., 2019). To understand this discrepancy, we consider the carbon isotope mass balance of a region affected by a persistent $\Delta^{14}C$ anomaly: First, a larger volume ($\boldsymbol{V}$) of affected water requires more ^{14}C-free geologic carbon input ($\Delta\boldsymbol{C}$) to attain a given $\Delta^{14}C$ anomaly ($\boldsymbol{A}$) against the background seawater DIC. Second, and more importantly, maintaining this anomaly ($\frac{\boldsymbol{\delta A}}{\boldsymbol{\delta t}} = \boldsymbol{0}$) against mixing ($\boldsymbol{M}$) with the global ocean requires a persistent flux ($\boldsymbol{F}$) of geologic carbon that is reciprocal to the flushing timescale ($\boldsymbol{\tau} = \frac{\boldsymbol{V}}{\boldsymbol{M}}$) of the affected volume, but not the volume itself.

$$\Delta C \approx \frac{-A}{A+1} * V * DIC$$

$$\frac{\delta A}{\delta t} = 0 = F - \frac{\Delta C}{V} * M = F - \frac{\Delta C}{\tau}$$

$$\int F * \delta t = \Delta C * \frac{\Delta t}{\tau}$$

The key insight from this consideration is that a relatively sizable region of affected water requires a substantial amount of initial carbon release (ΔC) to develop observed anomalies (i.e., A of -0.2≈ -200‰), but the cumulative release needed to sustain these anomalies depends primarily on the flushing timescale. For example, generating a ~200% anomaly across a 100m depth interval of the North Pacific thermocline ($V \approx 8 \times 10^{15}\ m^3$) or the GoC ($V \approx 1.45 \times 10^{14}\ m^3$) requires an initial carbon input of 48 Pg C and 0.84 Pg C, respectively. Sustaining these anomalies for 1000 years against 1 Sv of exchange, however, requires 189 Pg C cumulative release in both cases, as the larger volume is flushed more slowly (254 years) than the smaller one (4.6 years)

Our results demonstrate the observed ETNP $\Delta^{14}C$ anomalies can be sustained in a region the size of the GoC, even with relatively short flushing timesclaes (τ < 5 years, Fig. 4a). In contrast, producing comparable anomalies in a larger region would require decades-long isolation that may be incompatible with known Pacific circulation. These findings suggest that the ETNP shadow zone's reduced ventilation made it uniquely susceptible to sustained $\Delta^{14}C$ depletion, consistent with the observed spatial clustering of reconstructed $\Delta^{14}C$ anomalies.

Zonal oxygen supply estimates suggest a mean flushing time of 17 years for the eastern tropical Pacific oxygen deficient zones (ODZs north and south of the equator; Sonnerup et al., 2019), and CFC-derived ventilation ages for the ETNP exceed 30 years on the 26.8 isopycnal (Fine et al., 2001). As of 1999, there was a sharp CFC front on the 26.8 isopycnal adjacent to Baja California, with concentrations dropping from 0.5 pmol kg^{-1} at 28˚N to 0.1 pmol kg^{-1} at 24˚N (van Geen et al., 2006), placing the Marchitto site and GoC into the most isolated corner of the ETNP shadow zone. Additionally, the reconstructed expansion of the ETNP ODZ during the deglacial period (Ganeshram & Pedersen, 1998; Gardner et al., 1997; Keigwin & Jones, 1990; Lyle et al., 1996; Studer et al., 2021) is consistent with hydrographically restricted oxygen and CFC flow from the subpolar North Pacific to Baja California. This hydrodynamic isolation predisposes the region to develop large $\Delta^{14}C$ anomalies, and any deglacial reduction in flushing time would proportionally decrease the required carbon release to drive $\Delta^{14}C$ anomalies. This mechanism could plausibly apply also to other ridge-proximal sites with $\Delta^{14}C$ anomalies in partially isolated settings, such as the Arabian sea (Bryan et al., 2010) or the North Atlantic under stadial climate conditions (Thornalley et al., 2011, 2015).

Our explanation for the ETNP is in contrast with other Pacific sites where large $\Delta^{14}C$ anomalies have been reported without significant isolation from the basin-wide circulation (Bova et al., 2018; Ronge et al., 2016; Stott et al., 2009). In these cases, anomalies may be highly localized to

the point of carbon release or reflect porewaters within the sediment column. For example, in the case of Galapagos, large $\Delta^{14}C$ anomalies in benthic foraminifera (living in the top few centimeters of sediment) coincide with no $\Delta^{14}C$ anomalies in nearby deep-sea corals (living on hard seafloor substrates and therefore directly sampling bottom water $\Delta^{14}C$, unlike benthic foraminifera; Chen et al., 2020).

While our optimized release histories appear as stadial- and interstadial-timed millennial-timescale pulses (Fig. 3), these should be viewed as schematic outcomes of the optimization rather than literal reconstructions of forcing. The intent of our approach is to bracket the fluxes required under different flushing regimes, not to prescribe climate-paced inputs. More realistically, ridge-related carbon fluxes likely increased more broadly during deglaciation in response to sea-level change (Huybers & Langmuir, 2009; David C. Lund & Asimow, 2011). In our model ensemble we did not optimize flushing time for a given assumed pulse geologic carbon, but we show that the total amount of carbon release required to meet observed $\Delta^{14}C$ anomalies depends critically on regional circulation changes (Fig. 4a). As such, we deem it more likely that the millennial-timescale structure of the ETNP $\Delta^{14}C$ anomaly responds to changes in regional circulation, rather than reflecting directly the time evolution of the geologic carbon source.

4.2 Carbon cycle implications

We find no discernable change in reconstructed seawater pH associated with severe $\Delta^{14}C$ anomalies in benthic and planktic foraminifera from the GoC (Fig. 4b), consistent with the recent discovery of carbon-rich, pH-neutral and $CaCO_3$-forming hydrothermal vents in the southern GoC (Paduan et al., 2018). The expected regional pH anomaly (ΔpH) and its effect on seafloor $CaCO_3$ saturation (ΔlnΩ) depend on the ambient seawater carbonate ion concentration ($[CO_3^{2-}]$ of 50-80 µmol kg^{-1}) and the difference in carbon and alkalinity release fluxes (F_{CO2} minus F_{ALK}) divided by the flushing timescale ($\boldsymbol{\tau}$):

$$\mathbf{2.3} * \Delta \boldsymbol{pH} \approx \Delta \boldsymbol{ln\Omega} = \frac{\boldsymbol{CPF}}{[\boldsymbol{CO_3^{2-}}]} * \frac{\boldsymbol{F_{CO_2} - F_{ALK}}}{\boldsymbol{\tau}}$$

Here, CPF (carbonate proton fraction) equates to the fraction of total seawater buffering due to the bicarbonate/carbonate buffer (Hain et al., 2015). The absence of a pH anomaly or signs of corrosion in our foraminifera samples suggests nearly equimolar CO_2 and alkalinity fluxes ($F_{CO2} \approx F_{ALK}$; i.e. carbon release predominantly in the form of bicarbonate ion), consistent with the hypothesized 'neutralized carbon' release as the source of the ETNP $\Delta^{14}C$ anomalies (Green et al., 2024; Rafter et al., 2019).

Once globally dissipated, equimolar carbon and alkalinity release would minimally affect deep-ocean Ω and cause only a small atmospheric CO_2 rise ($\Delta \ln CO_2$) after accounting for $CaCO_3$ compensation:

$$\Delta \boldsymbol{lnCO_2} \approx \frac{\mathbf{0.06\%}}{\boldsymbol{Pmol}} * \left(\mathbf{2} * \int \boldsymbol{F_{CO_2}} - \int \boldsymbol{F_{ALK}} \right)$$

where the scaling factors account for seawater buffering and equilibration with a finite atmosphere (Hain & Sigman, 2024). For example, the cumulative release of 800 Pg geologic carbon as 67 Pmol CO_2 would cause severe ocean acidification and 67 Pmol net $CaCO_3$ dissolution, resulting in an ~8% CO_2 rise. In contrast, an equimolar CO_2 and alkalinity release would be pH neutral, cause no $CaCO_3$ dissolution, and raise CO_2 by only 4%, consistent with the +12 ppm CO_2 rise in our simulated slow-flushing scenario (Fig. 3e). Thus, neutralized carbon release can explain the pH-neutral ETNP $\Delta^{14}C$ anomalies. Still, even when taken to the likely limit of the global ^{14}C budget constraint (Green et al., 2024), it would contribute only modestly to the +47% observed deglacial CO_2 rise. In this scenario, $\Delta^{14}C$ anomalies remain concentrated in the ETNP shadow zone, without significantly impacting radiocarbon dating to reconstruct ocean circulation in the rest of the global ocean.

5 Conclusions

Our coupled regional–global box model demonstrates that the large $\Delta^{14}C$ anomalies observed in the ETNP during the last deglaciation can be explained by geologic carbon release into a hydrodynamically isolated shadow zone. We show that a cumulative release of ~800 Pg of carbon—consistent with global radiocarbon budget constraints—is sufficient to reproduce the anomalies if residence times exceed a few years.

Boron isotope reconstructions from the Gulf of California indicate no corresponding pH anomaly, supporting a pH-neutral, alkalinity-bearing carbon source. Our results suggest that carbon was released primarily as bicarbonate rather than CO_2, allowing for both preservation of seafloor carbonate and minimal impact on atmospheric CO_2.

These findings reinforce the hypothesis of neutralized geologic carbon release during the deglacial period and demonstrate how regional ocean isolation can amplify local isotopic signals without overprinting the global ocean signal. As such, the ETNP $\Delta^{14}C$ anomalies may reflect a localized carbon cycle perturbation that is consistent with both observational constraints and global mass balance. This supports the continued use of $\Delta^{14}C$ as a tracer for global ocean circulation change, provided regional anomalies are carefully considered.

Acknowlegements

This research was supported by the National Science Foundation (NSF) through collaborative research grants OCE-2032340 (to M.P.H.) and OCE-20132340 (to P.A.R.). Additional support was provided by NSF grants OCE-1636005, AGS-2303599, and OCE-2503657 (to P.A.R.). J.W.B.R. was supported by NERC grant NE/N011716/1. We thank the Associate Editor as well as Dave Lund and two other anonymous reviewers for their thoughtful comments, which greatly improved this manuscript.

Conflict of Interest Statement

The authors have no conflicts of interest to disclose.

Open Research

The model code, plotting scripts, model output, and newly compiled $\delta^{13}C$, $\Delta^{14}C$, and $\delta^{11}B$ data used in this study are openly archived on Zenodo at (Green & csun365, 2025) and are also available via GitHub (https://github.com/RyanAGreen/GoCmodel).

References

Barker, S., Greaves, M., & Elderfield, H. (2003). A study of cleaning procedures used for foraminiferal Mg/Ca paleothermometry. *Geochemistry, Geophysics, Geosystems*, *4*(9). https://doi.org/10.1029/2003GC000559

Bereiter, B., Eggleston, S., Schmitt, J., Nehrbass-Ahles, C., Stocker, T. F., Fischer, H., et al. (2015). Revision of the EPICA Dome C CO2 record from 800 to 600 kyr before present. *Geophysical Research Letters*, *42*(2), 542–549. https://doi.org/10.1002/2014GL061957

Bereiter, B., Shackleton, S., Baggenstos, D., Kawamura, K., & Severinghaus, J. (2018). Mean global ocean temperatures during the last glacial transition. *Nature*, *553*(7686), 39–44. https://doi.org/10.1038/nature25152

Bolin, B. (1960). On the Exchange of Carbon Dioxide between the Atmosphere and the Sea. *Tellus*, *12*(3), 274–281. https://doi.org/10.3402/tellusa.v12i3.9402

Bova, S. C., Herbert, T. D., & Altabet, M. A. (2018). Ventilation of Northern and Southern Sources of Aged Carbon in the Eastern Equatorial Pacific During the Younger Dryas Rise in Atmospheric CO2. *Paleoceanography and Paleoclimatology*, *33*(11), 1151–1168. https://doi.org/10.1029/2018PA003386

Broecker, W., & Barker, S. (2007). A 190‰ drop in atmosphere's Δ14C during the "Mystery Interval" (17.5 to 14.5 kyr). *Earth and Planetary Science Letters*, *256*(1–2), 90–99. https://doi.org/10.1016/j.epsl.2007.01.015

529 Bryan, S. P., Marchitto, T. M., & Lehman, S. J. (2010). The release of 14C-depleted carbon from the deep ocean
530 during the last deglaciation: Evidence from the Arabian Sea. *Earth and Planetary Science Letters*, *298*(1),
531 244–254. https://doi.org/10.1016/j.epsl.2010.08.025
532 Chen, T., Robinson, L. F., Burke, A., Claxton, L., Hain, M. P., Li, T., et al. (2020). Persistently well-ventilated
533 intermediate-depth ocean through the last deglaciation. *Nature Geoscience*, *13*(11), 733–738.
534 https://doi.org/10.1038/s41561-020-0638-6
535 Cook, M. S., & Keigwin, L. D. (2015). Radiocarbon profiles of the NW Pacific from the LGM and deglaciation:
536 Evaluating ventilation metrics and the effect of uncertain surface reservoir ages. *Paleoceanography*, *30*(3),
537 174–195. https://doi.org/10.1002/2014PA002649
538 Cook, M. S., Keigwin, L. D., Birgel, D., & Hinrichs, K.-U. (2011). Repeated pulses of vertical methane flux
539 recorded in glacial sediments from the southeast Bering Sea. *Paleoceanography*, *26*(2).
540 https://doi.org/10.1029/2010PA001993
541 Craig, H. (1957). The Natural Distribution of Radiocarbon and the Exchange Time of Carbon Dioxide Between
542 Atmosphere and Sea. *Tellus*, *9*(1), 1–17. https://doi.org/10.3402/tellusa.v9i1.9078
543 Dickson, A. G. (1990). Thermodynamics of the dissociation of boric acid in synthetic seawater from 273.15 to
544 318.15 K. *Deep Sea Research Part A. Oceanographic Research Papers*, *37*(5), 755–766.
545 https://doi.org/10.1016/0198-0149(90)90004-F
546 Fine, R. A., Maillet, K. A., Sullivan, K. F., & Willey, D. (2001). Circulation and ventilation flux of the Pacific
547 Ocean. *Journal of Geophysical Research: Oceans*, *106*(C10), 22159–22178.
548 https://doi.org/10.1029/1999JC000184
549 Foster, G. L. (2008). Seawater pH, pCO2 and [CO2- 3] variations in the Caribbean Sea over the last 130 kyr: A
550 boron isotope and B/Ca study of planktic foraminifera. *Earth and Planetary Science Letters*, *271*(1–4),
551 254–266.
552 Foster, G. L., Hönisch, B., Paris, G., Dwyer, G. S., Rae, J. W., Elliott, T., et al. (2013). Interlaboratory comparison
553 of boron isotope analyses of boric acid, seawater and marine CaCO3 by MC-ICPMS and NTIMS.
554 *Chemical Geology*, *358*, 1–14.
555 Frank, M., Eckhardt, J.-D., Eisenhauer, A., Kubik, P. W., Dittrich-Hannen, B., Segl, M., & Mangini, A. (1994).
556 Beryllium 10, thorium 230, and protactinium 231 in Galapagos microplate sediments: Implications of

hydrothermal activity and paleoproductivity changes during the last 100,000 years. *Paleoceanography*, *9*(4), 559–578. https://doi.org/10.1029/94PA01132

Ganeshram, R. S., & Pedersen, T. F. (1998). Glacial-interglacial variability in upwelling and bioproductivity off NW Mexico: Implications for Quaternary paleoclimate. *Paleoceanography*, *13*(6), 634–645. https://doi.org/10.1029/98PA02508

Garcia, H. E., Wang, Z., Bouchard, C., Cross, S. L., Paver, C. R., Reagan, J. R., et al. (2023). World Ocean Atlas 2023, Volume 3: Dissolved Oxygen, Apparent Oxygen Utilization, Dissolved Oxygen Saturation and 30-year Climate Normal. Retrieved from https://repository.library.noaa.gov/view/noaa/60601

Gardner, J. V., Dean, W. E., & Dartnell, P. (1997). Biogenic sedimentation beneath the California Current System for the past 30 kyr and its paleoceanographic significance. *Paleoceanography*, *12*(2), 207–225. https://doi.org/10.1029/96PA03567

van Geen, A., Smethie Jr., W. M., Horneman, A., & Lee, H. (2006). Sensitivity of the North Pacific oxygen minimum zone to changes in ocean circulation: A simple model calibrated by chlorofluorocarbons. *Journal of Geophysical Research: Oceans*, *111*(C10). https://doi.org/10.1029/2005JC003192

Gómez-Valdivia, F., Parés-Sierra, A., & Flores-Morales, A. L. (2015). The Mexican Coastal Current: A subsurface seasonal bridge that connects the tropical and subtropical Northeastern Pacific. *Continental Shelf Research*, *110*, 100–107.

Green, R. A., Hain, M. P., & Rafter, P. A. (2024). Deglacial Pulse of Neutralized Carbon From the Pacific Seafloor: A Natural Analog for Ocean Alkalinity Enhancement? *Geophysical Research Letters*, *51*(8), e2024GL108271. https://doi.org/10.1029/2024GL108271

Hain, M. P., & Sigman, D. M. (2024). CO2 in Earth's Ice Age Cycles. In *Oxford Research Encyclopedia of Climate Science*. https://doi.org/10.1093/acrefore/9780190228620.013.879

Hain, M. P., Sigman, D. M., & Haug, G. H. (2011). Shortcomings of the isolated abyssal reservoir model for deglacial radiocarbon changes in the mid-depth Indo-Pacific Ocean. *Geophysical Research Letters*, *38*(4). https://doi.org/10.1029/2010GL046158

Hain, M. P., Sigman, D. M., & Haug, G. H. (2014). Distinct roles of the Southern Ocean and North Atlantic in the deglacial atmospheric radiocarbon decline. *Earth and Planetary Science Letters*, *394*, 198–208. https://doi.org/10.1016/j.epsl.2014.03.020

585 Hain, M. P., Sigman, D. M., Higgins, J. A., & Haug, G. H. (2015). The effects of secular calcium and magnesium
586 concentration changes on the thermodynamics of seawater acid/base chemistry: Implications for Eocene
587 and Cretaceous ocean carbon chemistry and buffering. *Global Biogeochemical Cycles*, *29*(5), 517–533.
588 https://doi.org/10.1002/2014GB004986
589 Humphreys, M. P., Lewis, E. R., Sharp, J. D., & Pierrot, D. (2021). *PyCO2SYS v1.7: marine carbonate system*
590 *calculations in Python* (preprint). Oceanography. https://doi.org/10.5194/gmd-2021-159
591 Huybers, P., & Langmuir, C. (2009). Feedback between deglaciation, volcanism, and atmospheric CO2. *Earth and*
592 *Planetary Science Letters*, *286*(3), 479–491. https://doi.org/10.1016/j.epsl.2009.07.014
593 Keigwin, L. D., & Jones, G. A. (1990). Deglacial climatic oscillations in the Gulf of California. *Paleoceanography*,
594 *5*(6), 1009–1023. https://doi.org/10.1029/PA005i006p01009
595 Klochko, K., Kaufman, A. J., Yao, W., Byrne, R. H., & Tossell, J. A. (2006). Experimental measurement of boron
596 isotope fractionation in seawater. *Earth and Planetary Science Letters*, *248*(1), 276–285.
597 https://doi.org/10.1016/j.epsl.2006.05.034
598 Lauvset, S. K., Lange, N., Tanhua, T., Bittig, H. C., Olsen, A., Kozyr, A., et al. (2024). The annual update
599 GLODAPv2.2023: the global interior ocean biogeochemical data product. *Earth System Science Data*,
600 *16*(4), 2047–2072. https://doi.org/10.5194/essd-16-2047-2024
601 Lavín, M. F., & Marinone, S. G. (2003). An Overview of the Physical Oceanography of the Gulf of California. In O.
602 U. Velasco Fuentes, J. Sheinbaum, & J. Ochoa (Eds.), *Nonlinear Processes in Geophysical Fluid*
603 *Dynamics: A tribute to the scientific work of Pedro Ripa* (pp. 173–204). Dordrecht: Springer Netherlands.
604 https://doi.org/10.1007/978-94-010-0074-1_11
605 Lindsay, C. M., Lehman, S. J., Marchitto, T. M., & Ortiz, J. D. (2015). The surface expression of radiocarbon
606 anomalies near Baja California during deglaciation. *Earth and Planetary Science Letters*, *422*, 67–74.
607 https://doi.org/10.1016/j.epsl.2015.04.012
608 Lindsay, C. M., Lehman, S. J., Marchitto, T. M., Carriquiry, J. D., & Ortiz, J. D. (2016). New constraints on
609 deglacial marine radiocarbon anomalies from a depth transect near Baja California. *Paleoceanography*,
610 *31*(8), 1103–1116. https://doi.org/10.1002/2015PA002878

611 Lund, D. C., Asimow, P. D., Farley, K. A., Rooney, T. O., Seeley, E., Jackson, E. W., & Durham, Z. M. (2016).
612 Enhanced East Pacific Rise hydrothermal activity during the last two glacial terminations. *Science*,
613 *351*(6272), 478–482. https://doi.org/10.1126/science.aad4296
614 Lund, David C., & Asimow, P. D. (2011). Does sea level influence mid-ocean ridge magmatism on Milankovitch
615 timescales? *Geochemistry, Geophysics, Geosystems*, *12*(12). https://doi.org/10.1029/2011GC003693
616 Lund, David C., Pavia, F. J., Seeley, E. I., McCart, S. E., Rafter, P. A., Farley, K. A., et al. (2019). Hydrothermal
617 scavenging of 230Th on the Southern East Pacific Rise during the last deglaciation. *Earth and Planetary*
618 *Science Letters*, *510*, 64–72. https://doi.org/10.1016/j.epsl.2018.12.037
619 Lyle, M., Koizumi, I., Richter, C., Fox, P. J., Baldauf, J., & Francis, T. J. (1996). Ocean Drilling Program. Retrieved
620 from http://www-odp.tamu.edu/publications/prelim/167_prel/167prel.pdf
621 Marchitto, T. M., Lehman, S. J., Ortiz, J. D., Flückiger, J., & Van Geen, A. (2007). Marine Radiocarbon Evidence
622 for the Mechanism of Deglacial Atmospheric CO2 Rise. *Science*, *316*(5830), 1456–1459.
623 https://doi.org/10.1126/science.1138679
624 Nix, R. K. (2013). The Gulf of California. *A Physical, Geological and Biological Study. University of Texas, Dallas*.
625 Retrieved from
626 https://citeseerx.ist.psu.edu/document?repid=rep1&type=pdf&doi=4fda34a7425758aa17c3d0035676f87db
627 6f9f111
628 Paduan, J. B., Zierenberg, R. A., Clague, D. A., Spelz, R. M., Caress, D. W., Troni, G., et al. (2018). Discovery of
629 Hydrothermal Vent Fields on Alarcón Rise and in Southern Pescadero Basin, Gulf of California.
630 *Geochemistry, Geophysics, Geosystems*, *19*(12), 4788–4819. https://doi.org/10.1029/2018GC007771
631 Rae, J. W. B. (2018). Boron Isotopes in Foraminifera: Systematics, Biomineralisation, and CO2 Reconstruction. In
632 H. Marschall & G. Foster (Eds.), *Boron Isotopes* (pp. 107–143). Cham: Springer International Publishing.
633 https://doi.org/10.1007/978-3-319-64666-4_5
634 Rae, J. W. B., Foster, G. L., Schmidt, D. N., & Elliott, T. (2011). Boron isotopes and B/Ca in benthic foraminifera:
635 Proxies for the deep ocean carbonate system. *Earth and Planetary Science Letters*, *302*(3–4), 403–413.
636 https://doi.org/10.1016/j.epsl.2010.12.034

637 Rafter, P. A., Herguera, J.-C., & Southon, J. R. (2018). Extreme lowering of deglacial seawater radiocarbon
638 recorded by both epifaunal and infaunal benthic foraminifera in a wood-dated sediment core. *Climate of the*
639 *Past*, *14*(12), 1977–1989. https://doi.org/10.5194/cp-14-1977-2018
640 Rafter, P. A., Carriquiry, J. D., Herguera, J., Hain, M. P., Solomon, E. A., & Southon, J. R. (2019). Anomalous >
641 2000-Year-Old Surface Ocean Radiocarbon Age as Evidence for Deglacial Geologic Carbon Release.
642 *Geophysical Research Letters*, *46*(23), 13950–13960. https://doi.org/10.1029/2019GL085102
643 Rafter, P. A., Gray, W. R., Hines, S. K. V., Burke, A., Costa, K. M., Gottschalk, J., et al. (2022). Global
644 reorganization of deep-sea circulation and carbon storage after the last ice age. *Science Advances*, *8*(46),
645 eabq5434. https://doi.org/10.1126/sciadv.abq5434
646 Reimer, P. J., Austin, W. E. N., Bard, E., Bayliss, A., Blackwell, P. G., Ramsey, C. B., et al. (2020). The IntCal20
647 Northern Hemisphere Radiocarbon Age Calibration Curve (0–55 cal kBP). *Radiocarbon*, *62*(4), 725–757.
648 https://doi.org/10.1017/RDC.2020.41
649 Revelle, R., & Suess, H. E. (1957). Carbon Dioxide Exchange Between Atmosphere and Ocean and the Question of
650 an Increase of Atmospheric CO2 during the Past Decades. *Tellus*, *9*(1), 18–27.
651 https://doi.org/10.1111/j.2153-3490.1957.tb01849.x
652 Ronge, T. A., Tiedemann, R., Lamy, F., Köhler, P., Alloway, B. V., De Pol-Holz, R., et al. (2016). Radiocarbon
653 constraints on the extent and evolution of the South Pacific glacial carbon pool. *Nature Communications*,
654 *7*(1), 11487. https://doi.org/10.1038/ncomms11487
655 Ryan A. Green, & csun365. (2025). RyanAGreen/GoCmodel: v3.0 - Full archive: model, output, and observational
656 data (v3.0). [Software] Zenodo. https://doi.org/10.5281/zenodo.15588737
657 Skinner, L. C., Fallon, S., Waelbroeck, C., Michel, E., & Barker, S. (2010). Ventilation of the Deep Southern Ocean
658 and Deglacial CO2 Rise. *Science*, *328*(5982), 1147–1151. https://doi.org/10.1126/science.1183627
659 Sonnerup, R. E., Chang, B. X., Warner, M. J., & Mordy, C. W. (2019). Timescales of ventilation and consumption
660 of oxygen and fixed nitrogen in the eastern tropical South Pacific oxygen deficient zone from transient
661 tracers. *Deep Sea Research Part I: Oceanographic Research Papers*, *151*, 103080.
662 https://doi.org/10.1016/j.dsr.2019.103080
663 Stott, L., & Timmermann, A. (2011). Hypothesized Link Between Glacial/Interglacial Atmospheric CO2 Cycles and
664 Storage/Release of CO2-Rich Fluids From Deep-Sea Sediments. In H. Rashid, L. Polyak, & E. Mosley-

Thompson (Eds.), *Geophysical Monograph Series* (Vol. 193, pp. 123–138). Washington, D. C.: American Geophysical Union. https://doi.org/10.1029/2010GM001052

Stott, L., Southon, J., Timmermann, A., & Koutavas, A. (2009). Radiocarbon age anomaly at intermediate water depth in the Pacific Ocean during the last deglaciation. *Paleoceanography*, *24*(2), n/a-n/a. https://doi.org/10.1029/2008PA001690

Stott, L., Davy, B., Shao, J., Coffin, R., Pecher, I., Neil, H., et al. (2019). CO2 Release From Pockmarks on the Chatham Rise-Bounty Trough at the Glacial Termination. *Paleoceanography and Paleoclimatology*, *34*(11), 1726–1743. https://doi.org/10.1029/2019PA003674

Stott, L. D., Harazin, K. M., & Krupinski, N. B. Q. (2019). Hydrothermal carbon release to the ocean and atmosphere from the eastern equatorial Pacific during the last glacial termination. *Environmental Research Letters*, *14*(2), 025007. https://doi.org/10.1088/1748-9326/aafe28

Studer, A. S., Mekik, F., Ren, H., Hain, M. P., Oleynik, S., Martínez-García, A., et al. (2021). Ice Age-Holocene Similarity of Foraminifera-Bound Nitrogen Isotope Ratios in the Eastern Equatorial Pacific. *Paleoceanography and Paleoclimatology*, *36*(5), e2020PA004063. https://doi.org/10.1029/2020PA004063

Stuiver, M., & Polach, H. A. (1977). Discussion Reporting of 14C Data. *Radiocarbon*, *19*(3), 355–363. https://doi.org/10.1017/S0033822200003672

Thornalley, D. J. R., Barker, S., Broecker, W. S., Elderfield, H., & McCave, I. N. (2011). The Deglacial Evolution of North Atlantic Deep Convection. *Science*, *331*(6014), 202–205. https://doi.org/10.1126/science.1196812

Thornalley, D. J. R., Bauch, H. A., Gebbie, G., Guo, W., Ziegler, M., Bernasconi, S. M., et al. (2015). A warm and poorly ventilated deep Arctic Mediterranean during the last glacial period. *Science*, *349*(6249), 706–710. https://doi.org/10.1126/science.aaa9554

Trudgill, M., Nuber, S., Block, H. E., Crumpton-Banks, J., Jurikova, H., Littley, E., et al. (2024). A Simple, Low-Blank Batch Purification Method for High-Precision Boron Isotope Analysis. *Geochemistry, Geophysics, Geosystems*, *25*(3), e2023GC011350. https://doi.org/10.1029/2023GC011350

Virtanen, P., Gommers, R., Oliphant, T. E., Haberland, M., Reddy, T., Cournapeau, D., et al. (2020). SciPy 1.0: fundamental algorithms for scientific computing in Python. *Nature Methods*, *17*(3), 261–272. https://doi.org/10.1038/s41592-019-0686-2

692 Vogl, J., & Rosner, M. (2012). Production and Certification of a Unique Set of Isotope and Delta Reference
693 Materials for Boron Isotope Determination in Geochemical, Environmental and Industrial Materials.
694 *Geostandards and Geoanalytical Research*, *36*(2), 161–175. https://doi.org/10.1111/j.1751-
695 908X.2011.00136.x
696 Walczak, M. H., Mix, A. C., Cowan, E. A., Fallon, S., Fifield, L. K., Alder, J. R., et al. (2020). Phasing of
697 millennial-scale climate variability in the Pacific and Atlantic Oceans. *Science*, *370*(6517), 716–720.
698 https://doi.org/10.1126/science.aba7096
699 Xu, C., Jurikova, H., Nuber, S., Steele, R. C. J., Trudgill, M., Barker, S., et al. (2024). A Rapid, Simple, and Low-
700 Blank Pumped Ion-Exchange Column Chromatography Technique for Boron Purification From Carbonate
701 and Seawater Matrices. *Geochemistry, Geophysics, Geosystems*, *25*(2), e2023GC011228.
702 https://doi.org/10.1029/2023GC011228
703 Zeebe, R. E., & Wolf-Gladrow, D. (2001). *CO2 in seawater: equilibrium, kinetics, isotopes* (Vol. 65). Gulf
704 Professional Publishing. Retrieved from
705 https://books.google.com/books?hl=en&lr=&id=g3j3Zn4kEscC&oi=fnd&pg=PA1&dq=wolf+gladorw+zee
706 be&ots=ldTvKYtkyP&sig=gg0lC0nb84SxhMjD0kRvvMvnPH8
707

Figure 1.

A
younger than
2500 years
2576
2840
3753
4316
2651
7618
O2=20
O2=20
20
15
10
5
0
O2 (μmol kg-1)

B
120.0
60.0
120.0
60.0
2.0
1.5
1.0
0.5
0.0
CFC-11 (pmol kg-1)

Figure 2.

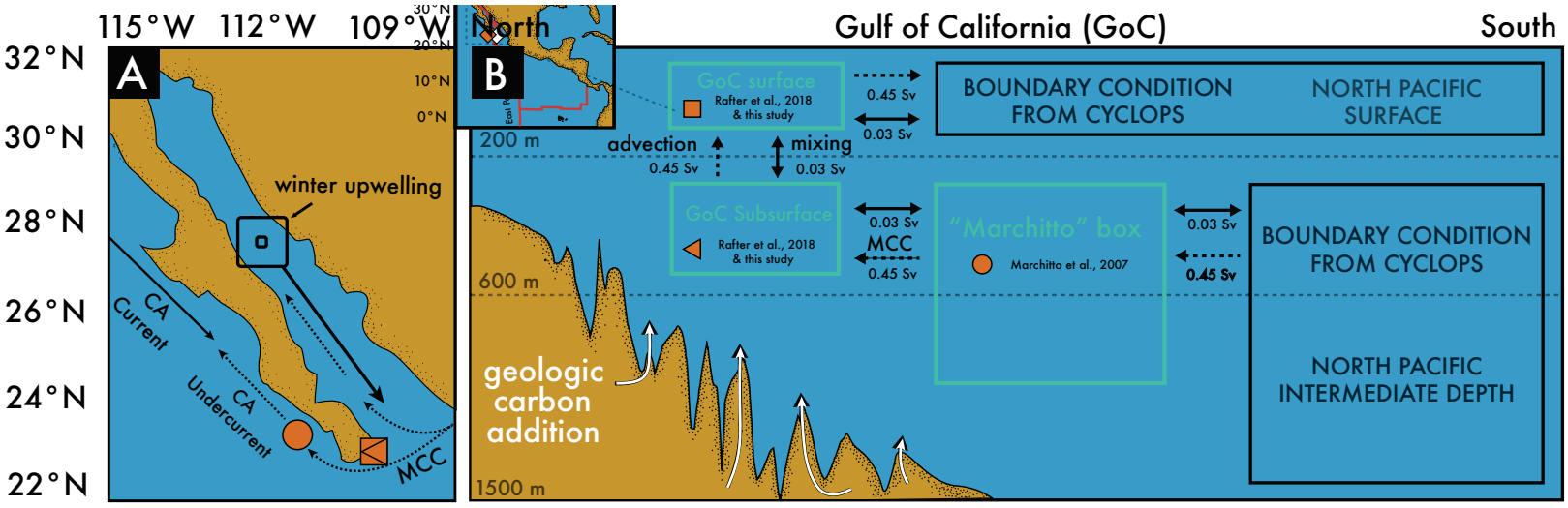
115°W
112°W
109°W
32°N
30°N
28°N
26°N
24°N
22°N
A
winter upwelling
CA Current
CA Undercurrent
MCC
B
North
Gulf of California (GoC)
South
GoC surface
Rafter et al., 2018 & this study
0.45 Sv
0.03 Sv
BOUNDARY CONDITION FROM CYCLOPS
NORTH PACIFIC SURFACE
200 m
advection
0.45 Sv
mixing
0.03 Sv
GoC Subsurface
Rafter et al., 2018 & this study
0.03 Sv
MCC
0.45 Sv
"Marchitto" box
Marchitto et al., 2007
0.03 Sv
0.45 Sv
BOUNDARY CONDITION FROM CYCLOPS
600 m
geologic carbon addition
NORTH PACIFIC INTERMEDIATE DEPTH
1500 m

Figure 3.

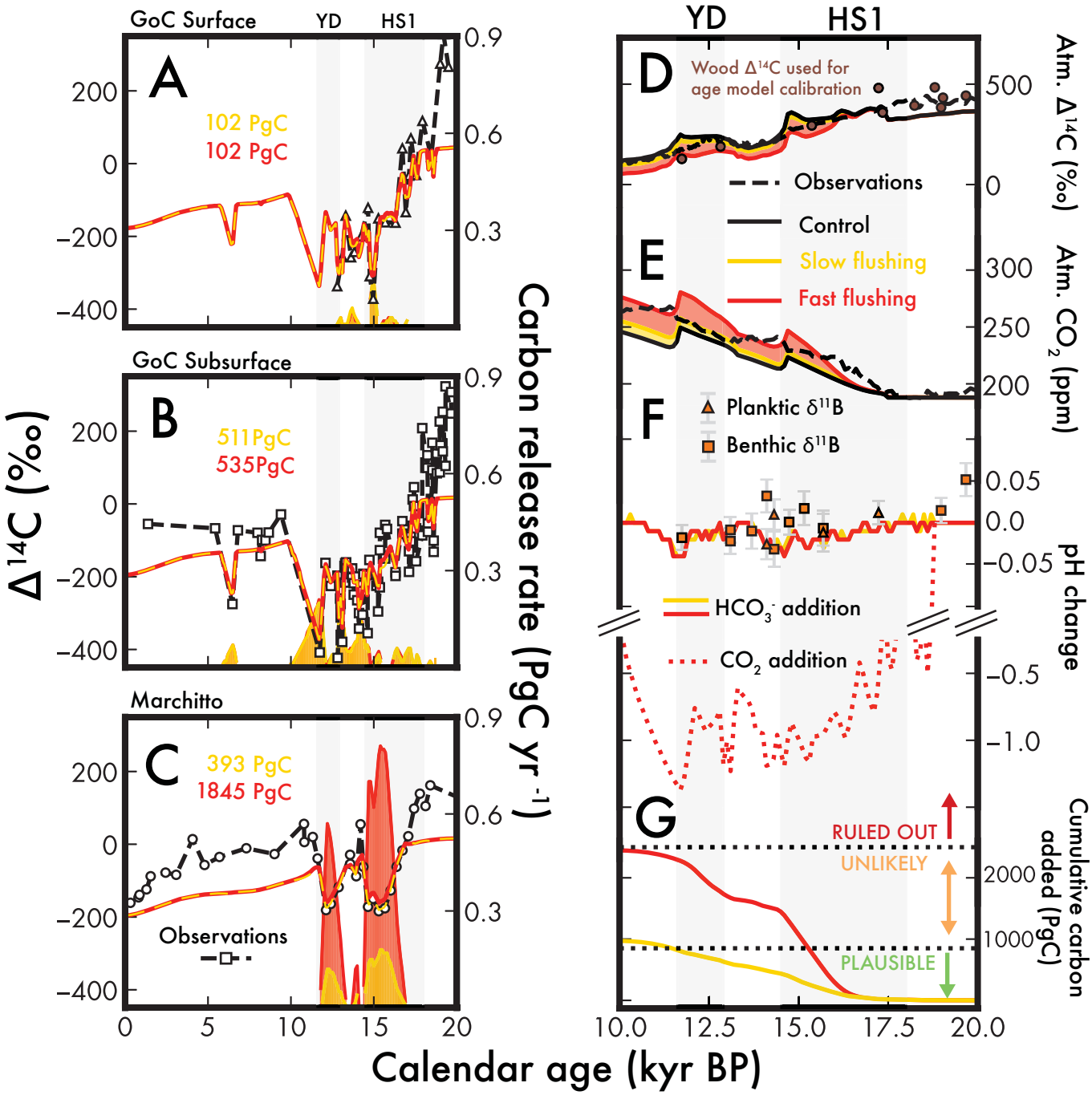
GoC Surface
YD
HS1
A
102 PgC
102 PgC
GoC Subsurface
B
511PgC
535PgC
Marchitto
C
393 PgC
1845 PgC
Observations
Δ14C (‰)
Carbon release rate (PgC yr-1)
Calendar age (kyr BP)
D
Wood Δ14C used for age model calibration
Observations
Control
Slow flushing
Fast flushing
Atm. Δ14C (‰)
E
Atm. CO2 (ppm)
F
Planktic δ11B
Benthic δ11B
HCO3- addition
CO2 addition
pH change
G
RULED OUT
UNLIKELY
PLAUSIBLE
Cumulative carbon added (PgC)

Figure 4.

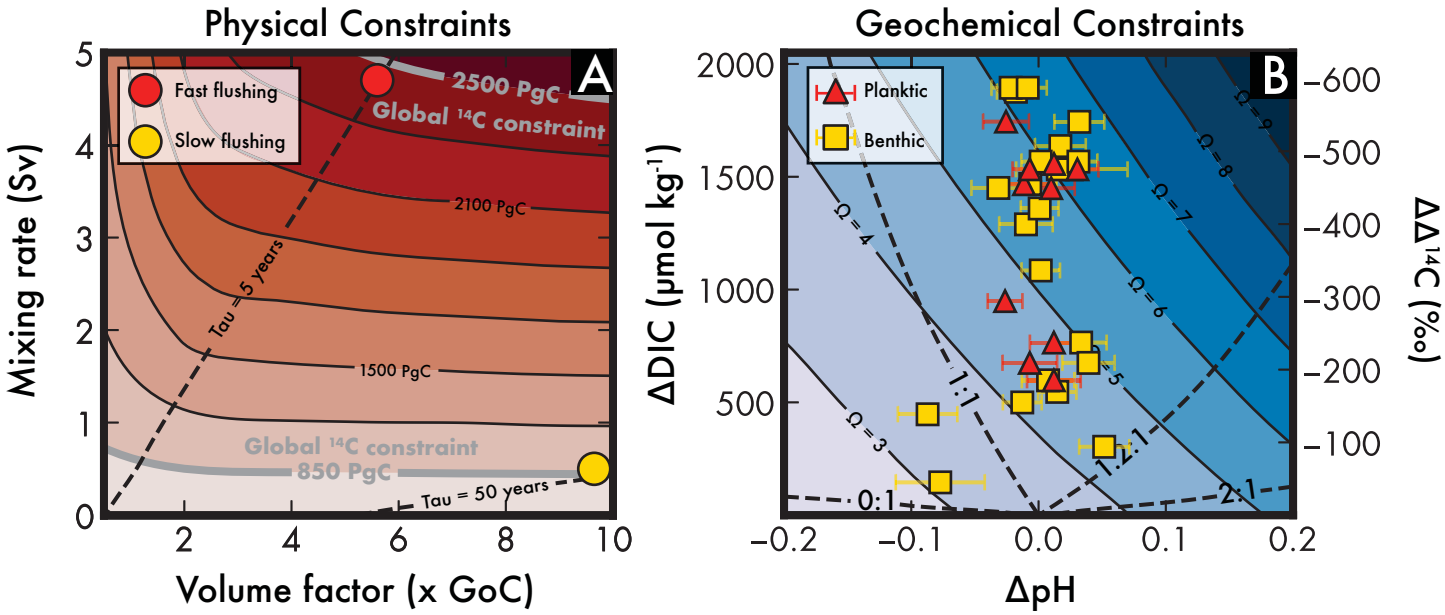
Physical Constraints
A
Fast flushing
Slow flushing
2500 PgC
Global ¹⁴C constraint
2100 PgC
Tau = 5 years
1500 PgC
Global ¹⁴C constraint
850 PgC
Tau = 50 years
Mixing rate (Sv)
Volume factor (x GoC)
0
1
2
3
4
5
2
4
6
8
10
Geochemical Constraints
B
Planktic
Benthic
Ω = 9
Ω = 8
Ω = 7
Ω = 6
Ω = 5
Ω = 4
Ω = 3
1:1
1:2:1
2:1
0:1
ΔDIC (µmol kg⁻¹)
ΔpH
ΔΔ¹⁴C (‰)
500
1000
1500
2000
−0.2
−0.1
0.0
0.1
0.2
−100
−200
−300
−400
−500
−600